Lawrence Berkeley National Laboratory

Title

Quantifying the topology of magnetic skyrmions in three dimensions.

Permalink

https://escholarship.org/uc/item/8jz4q19m

Journal

Science Advances, 10(40)

Authors

Raftrey, David

Finizio, Simone

Chopdekar, Rajesh

et al.

Publication Date

2024-10-04

DOI

10.1126/sciadv.adp8615

Peer reviewed

CONDENSED MATTER PHYSICS

Quantifying the topology of magnetic skyrmions in three dimensions

David Raftrey[1,2], Simone Finizio[3], Rajesh V. Chopdekar[4], Scott Dhuey[5], Temuujin Bayaraa[1], Paul Ashby[5], Jörg Raabe[3], Tiffany Santos[4], Sinéad Griffin[1,5], Peter Fischer[1,2]*

Magnetic skyrmions have so far been treated as two-dimensional spin structures characterized by a topological winding number. However, in real systems with the finite thickness of the device material being larger than the magnetic exchange length, the skyrmion spin texture extends into the third dimension and cannot be assumed as homogeneous. Using soft x-ray laminography, we reconstruct with about 20-nanometer spatial (voxel) size the full three-dimensional spin texture of a skyrmion in an 800-nanometer-diameter and 95-nanometer-thin disk patterned into a 30× [iridium/cobalt/platinum] multilayered film. A quantitative analysis finds that the evolution of the radial profile of the topological skyrmion number is nonuniform across the thickness of the disk. Estimates of the micromagnetic energy densities suggest that the changes in topological profile are related to nonuniform competing energetic interactions. Our results provide a foundation for nanoscale metrology for spintronics devices using topology as a design parameter.

INTRODUCTION

The description of magnetic skyrmions as two-dimensional (2D) objects has provided an enormous insight into their properties, behavior, and functionality, specifically toward the exploration of magnetic skyrmions in future spintronics applications. However, in real systems with a finite thickness larger than the magnetic exchange length, the details of the spin texture extending into the third dimension cannot be neglected. One cannot assume that a skyrmion extends into the third dimension simply as a rigid skyrmion tube as there is an additional dimension for evolution into a more complex 3D spin texture. Advanced synthesis methods allow a highly precise engineering of materials that extend into the third dimension, and, therefore, a fundamental understanding of the full 3D spin texture opens opportunities to explore and tailor 3D topological spintronic devices with enhanced functionalities that cannot be achieved in two dimensions. Spin textures including skyrmion tubes (*1*, *2*), hopfions (*3*, *4*), torons, cocoons (*5*), vortex rings (*6*), and ferroelectric polar skyrmions (*7*) and artificially designed magnetic nanostructures, such as twisted wires, tetrapods, etc., are among these 3D topological building blocks that are currently receiving substantial interest (*8–11*).

Magnetic skyrmions are particle-like topological solitons, where the magnetization in the center of the skyrmion points in the opposite direction of its surrounding magnetization. They are indexed by a topological charge: the skyrmion number or winding number. The winding number is defined as $N_{sk} = \frac{1}{4\pi} \iint \mathbf{m} \cdot \left(\frac{\partial \mathbf{m}}{\partial x} \times \frac{\partial \mathbf{m}}{\partial y} \right) dxdy$ with $\mathbf{m}$ being the magnetization. N_{sk} counts how many times the direction of a spin wraps around a unit sphere, converging to $N_{sk} = 1$ for a magnetic skyrmion.

The presence of skyrmions or other magnetic textures at the microscopic level fundamentally determines the properties, behavior, and functionality of magnetic materials. The energetic magnetic ground state is a result of competing magnetic interactions or energies. The symmetric exchange (Heisenberg) interaction favors a parallel or antiparallel alignment of neighboring spins, and the antisymmetric exchange (Dzyaloshinskii-Moriya) interaction (DMI) favors noncollinear spin arrangements, both of which are short range, whereas the dipolar interaction is a long-range interaction. The magnetocrystalline anisotropy energy originates from the orbital moment, and the Zeeman energy is proportional to any external magnetic fields that the material experiences.

A prerequisite toward the development of these 3D spintronics is advanced characterization techniques that address energetic contributions and topology. Several approaches using magnetic tomography techniques are emerging using advanced electron and x-ray–based microscopies. Real-space x-ray microscopy such as full-field transmission soft x-ray microscopy and diffraction-based x-ray techniques, including x-ray ptychography and x-ray laminography, all use x-ray magnetic dichroism effects as strong, element-specific, and quantitative magnetic contrast to provide 3D images with a high level of detail that are among the most promising approaches (*12*). Here, we use soft x-ray laminography to obtain a quantitative analysis of the 3D spin texture of a magnetic skyrmion in a multilayered disk with 800 nm in diameter and 95 nm in thickness and measure the depth-dependent radial profile of the skyrmion number.

RESULTS

The system used in this experiment is a magnetic multilayer of Ir/Co/Pt patterned into a disk (Fig. 1A). This class of multilayers is an established platform and is particularly appealing as it offers sensitive responses of the spin texture to changes and orderings of the thicknesses of the layers leading to topological textures such as skyrmions (*13*), target skyrmions (*14*), and hopfions (*3*, *4*). The origin of the topological textures in this system is the inversion symmetry breaking of the trilayer stack, which gives rise to a DMI interaction at the interface. In addition to DMI, the spin-orbit coupling between the Co and Pt at the interface creates an (out-of-plane) perpendicular

[1]Materials Sciences Division, Lawrence Berkeley National Laboratory, Berkeley, CA 94720, USA. [2]Physics Department, University of California Santa Cruz, Santa Cruz, CA 95064, USA. [3]Swiss Light Source, Paul Scherrer Institute, 5232 Villigen PSI, Switzerland. [4]Western Digital Research Center, Western Digital Corporation, San Jose, CA 95119, USA. [5]Molecular Foundry, Lawrence Berkeley National Laboratory, Berkeley, CA 94720, USA.
*Corresponding author. Email: pjfischer@lbl.gov
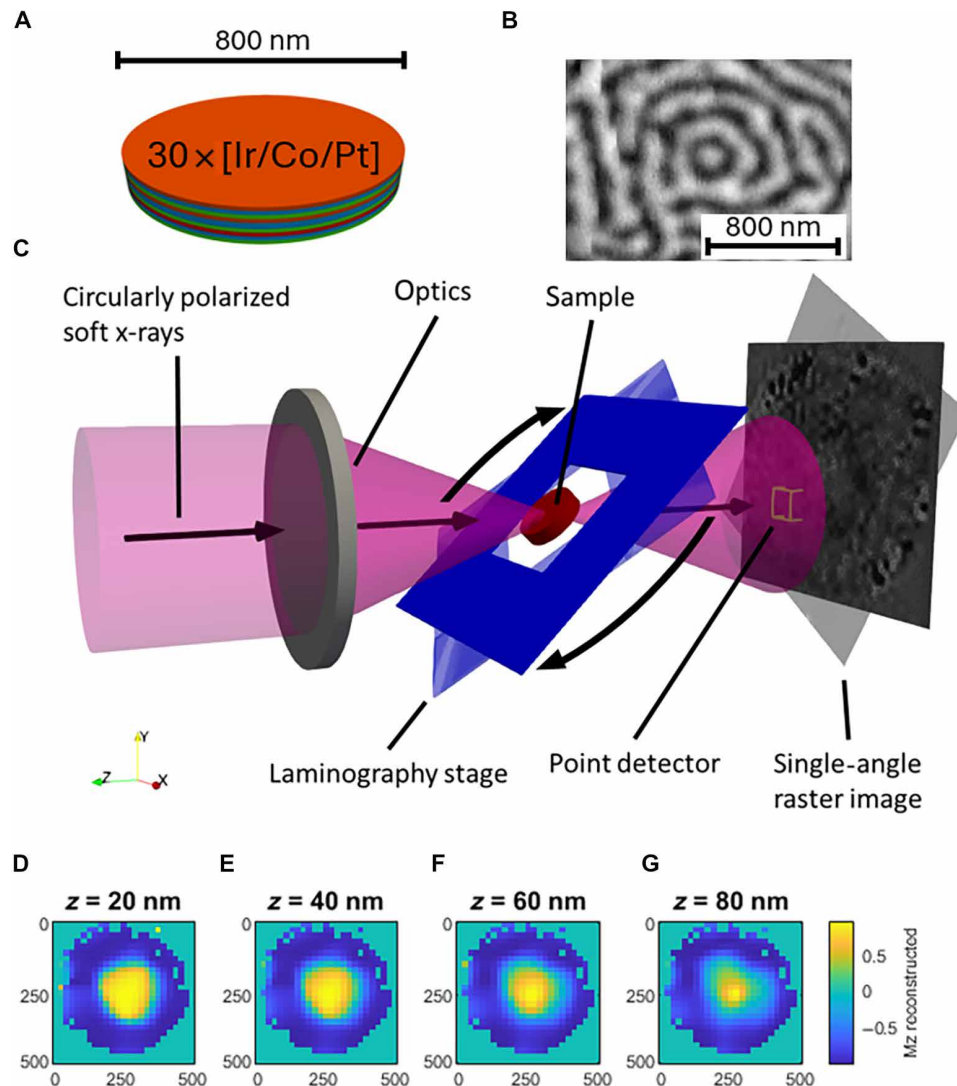
Fig. 1. Experimental schematic. (**A**) Scale schematic of the magnetic multilayer disk used in the x-ray experiment. The disk was deposited on a 100-nm-thin SiNx membrane. (**B**) Magnetic force microscopy phase shift image of an unpatterned film with the same composition as the disk used for the laminography reconstruction. A topological target skyrmion is visible in the magnetic force microscopy image. (**C**) A schematic of the Pollux laminography beamline at the Swiss Light Source. The sample is mounted on a rotary stage for the measurements. (**D** to **G**) Reconstructed single magnetization images calculated from all projection angles through the reconstruction. The layer-wise resolution shows the z-resolved variation in the skyrmion texture. The full stack is used to create the 3D rendering.

magnetic anisotropy (PMA) (*15*). Previous studies have established that the DMI and PMA depend on layer thicknesses and ordering (*16*).

With this type of multilayer system (Ir/Co/Pt), the ability to control the system properties through layer thicknesses means that the third dimension must be considered. In particular, in the case of nanopatterned elements, as in this study, the lateral dimension is on the same length scale as the height of the disk. Previously reported studies in these systems made with electron microscope imaging on the several nanometer length scale (*2*) and with hard x-rays on the micrometer length scale (*6*, *17*) observed complex 3D spin textures. Several-nanometer element–specific soft x-ray imaging with scanning transmission x-ray microscopy (STXM) has the advantages of element specificity as compared to electron imaging and much faster acquisition time compared to hard x-rays due to the resonant enhancement of the magnetic circular dichroism at L_2 and L_3 edges. In

particular, for 3D time-resolved experiments, the faster acquisition time of soft x-ray STXM is a necessity (*18*). The combination of multilayer engineering, structural imprinting, and soft x-ray laminography imaging allows us to probe the microstructure at a length scale relevant for deducing micromagnetic parameters and energy densities within the spin textures with implication for nucleation and stability.

Images from 56 rotation covering 360° are used to reconstruct a 3D vectorized rendering. An iterative solver first creates a reconstruction of the topography of the disk. The 3D topographic information is then used in a second step of the reconstruction algorithm, from which the spatially resolved magnetization vector field is obtained (Fig. 2A). Additional details on the reconstruction algorithms used for magnetic laminography can be found in (*17*). Each vector component ($\mathbf{m}_x$, $\mathbf{m}_y$, $\mathbf{m}_z$) was reconstructed separately
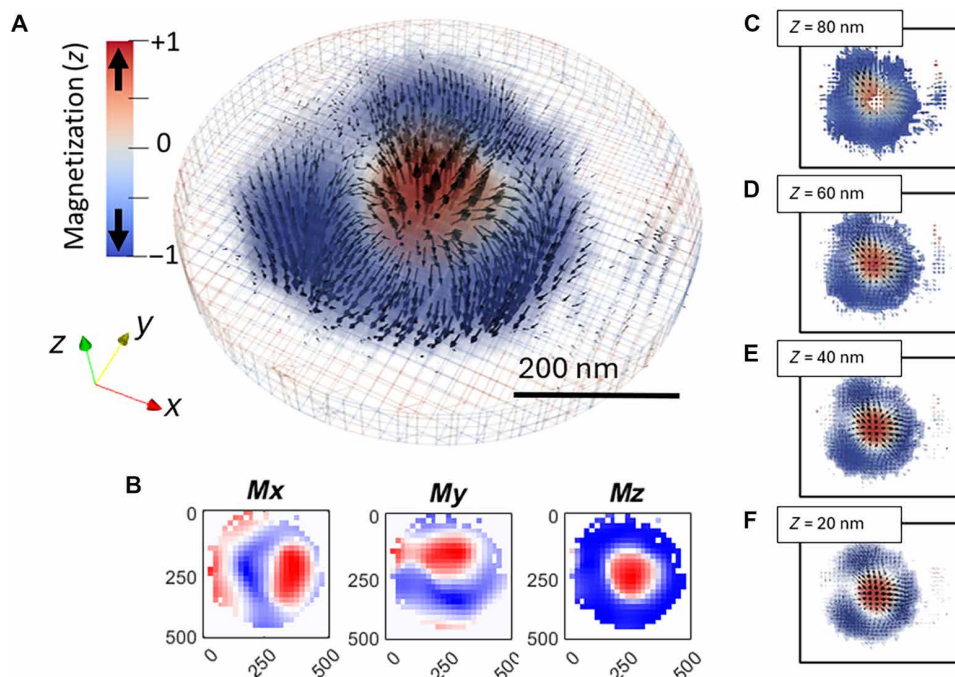
Fig. 2. 3D reconstruction. (**A**) A rendering in paraview of the product of the 3D reconstruction. The region of high statistical confidence contrast is ~500 nm of the full 800-nm diameter of the disk. Blue-red color scaling maps the *z* component of magnetization with red up and blue down. (**B**) *z*-axis projections of individual Cartesian magnetization components. (**C** to **F**) Individual 20-nm resolved slices along *z* axis showing depth evolution of the skyrmion.

(Fig. 2B) and then combined to produce the full 3D vector field (Fig. 2A). The reconstruction algorithm produces slices along the *z* axis with a thickness of 20 nm that can be used to analyze the data in three dimensions. The data are rendered using the visualization software ParaView.

Depth profile of the topological skyrmion number and chirality

With only a single projection axis, it is not possible to quantify the topological charge directly from the data. Typically, studies rely on theory-laden interpretation of data, often through indirect comparison between experimental data and projections of micromagnetic simulations.

Even for relatively thin systems, a 2D approximation does not capture important aspects as chirality is not always conserved along the depth profile because of flux-closure structures at the top and bottom of the film, e.g., Neél caps. Even several atomic layer differences in magnetic thin films may change chirality and topology (*19*). For intrinsically 3D structures such as hopfions (*3*) or dipolar skyrmions (*20*), the topological features can only be quantitatively probed by means of a 3D dataset. Several approaches have emerged with the capability of imaging topological magnetic structures at the resolution relevant to micromagnetic interactions and quantitative analysis of topological features including electron holography, x-ray ptychography, and, as in this work, soft x-ray laminography (*6, 21–23*).

We find that the profile of the topological charge across the disk has a depth dependence (Fig. 3A). The 3D data allow us to quantitatively compute the skyrmion number or topological charge directly from the data (Fig. 3A) in a discrete form. We find that, consistent with theory, the topological charge converges to a near-integer

value when integrated radially. This value converges for all depth-dependent layers. From the data, it is possible to produce a 3D rendering of the topological charge density, which is proportional to the fringing field of the spin texture. This fringing field is found to be the largest on the domain wall of the skyrmion where the rotation of the texture leads to noncollinear spins creating uncompensated volume charges (Fig. 3A).

A micromagnetic curve fitting approach was used to analyze the energetics of the system. The quantity of interest for this system is the topological charge density ρ_{sk}, which is the integrated spatial quantity in the skyrmion number integral $\rho_{sk} = \frac{1}{4\pi} \mathbf{m} \cdot \left(\frac{\partial \mathbf{m}}{\partial x} \times \frac{\partial \mathbf{m}}{\partial y} \right)$. The spin texture arises from the competition between different energetic interactions. By radially integrating the topological charge density in the disk, a topological profile across the depth can be compared to micromagnetic simulations to estimate the variation of the relative energetic contributions from the different interactions, i.e., PMA and DMI (Fig. 3, B and C).

The radial coordinate system is chosen because of the radial symmetry of the disk and nearly radial symmetry of the reconstructed texture. For the reconstructed skyrmion texture, variations from radial symmetry are apparent in the reconstructed image (Fig. 2A). Taking an integrated profile allows for comparison between simulated skyrmion profiles and reconstructed profiles by reducing the dimension of the data. The total integrated topological charge will converge to unity regardless of the chosen coordinate system.

Particularly important for topological quantities is the DMI interaction, which prefers noncollinear spins. The profile of the integrated topological charge density is fitted with the function $\frac{1}{\left(e^{-\alpha*(r+\rho)} + 1 \right)}$, with fitting parameters α and ρ, where α describes the profile shape and ρ is a shift in radial position, *r*. We find from
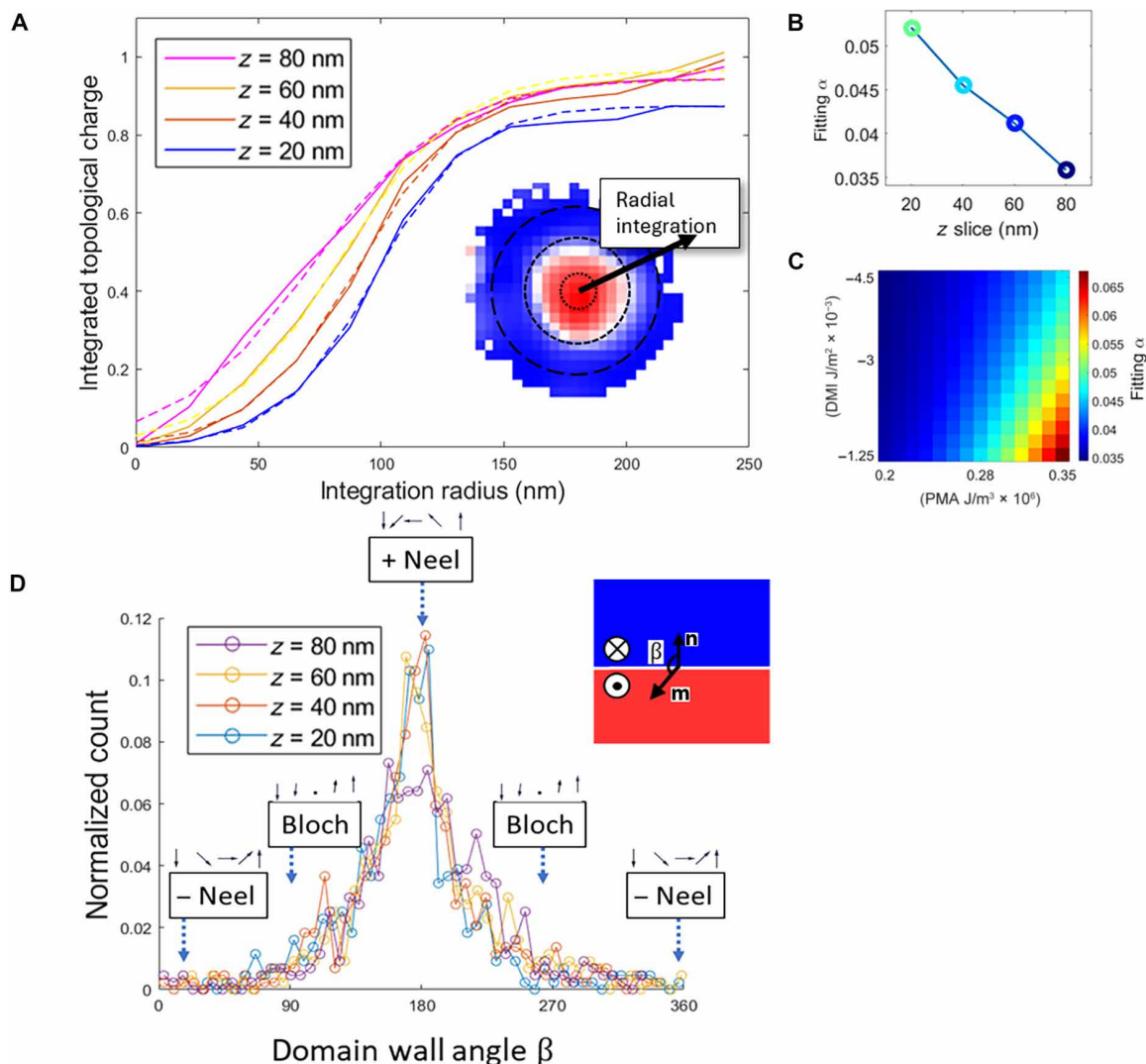
Fig. 3. Quantified topology and chirality. (**A**) Radially integrated topological charge profile across each depth in the reconstruction. Each curve is from a 20-nm-thick voxel slice of the reconstruction in z. Data are solid line, and fit is dashed line. (**B**) Fitting parameter α as a function of z position indicates a depth-dependent evolution of the spin texture's topological profile. (**C**) Micromagnetic simulations of a magnetic skyrmion spanning a phase space of DMI and PMA with the fitting parameter α plotted as a color scale. Simulations indicate that changes in micromagnetic energy terms may be responsible for the depth-dependent changes in fitting parameter. (**D**) Layer-resolved histogram of the chirality of the domain wall. The measured quantity at each voxel is the angle β between the domain wall normal and the in-plane component of the magnetization. Chirality is constant across the z profile indicating a positive chirality–valued Neél wall. The inset illustration shows chirality angle β of domain wall. The blue region represents a domain magnetized in $-z$, and the red region represents a domain magnetized in $+z$. The vector **n** is the normal vector, and **m** is the in-plane magnetization.

micromagnetic simulations that the fitting parameter α is inversely related to the skyrmion radius, which increases with increasing DMI and decreases with increasing anisotropy (Fig. 3, B and C). A larger skyrmion with a broader domain wall will have more spins canted that is preferred by the DMI. A skyrmion with a thin domain wall has the spins more perpendicular, following the out-of-plane anisotropy. The topological profile provides an especially well-defined curve for micromagnetic fitting procedures investigating the DMI versus PMA contribution. Using this curve, the depth dependence of energetics can be estimated. From the reconstruction, we find that the fitting parameter α is smallest at the top of the structure and largest at the bottom (Fig. 3B), suggesting a barrel-like profile similar to the depth profile of a vortex core (*24*). This suggests

that the DMI and PMA vary across the stack (Fig. 3C), which may be due to the changing interlayer roughness of successive layer depositions. The $z = 20$-nm layer does not converge to unity in the topological charge that may be due to numerical error of the reconstruction.

Chirality is another topological index that describes the rotation direction of the spins (*25*). The chirality quantitatively describes whether the domain wall is of Bloch or Neél type. The Bloch/Neél type is determined by crystal structure, and the sign of the chirality is determined by details of the spin-orbit interaction. Here, chirality is defined as the angle between the normal to the domain wall and the direction of the in-plane magnetization at the domain wall.

The chirality is quantified from data by first computing the gradient of the z component of the magnetization to find the normal vector to the domain wall, which lies in-plane. The angle between the normal vector and the in-plane components of magnetization is the chirality β. In the case of a Néel profile created by interfacial DMI, the angle is 180° in the case of positive chirality and 0° in the case of negative chirality. In the case of bulk-type DMI like in B20 compounds, the chirality is Bloch type with an angle of 90° or 270°. From the dataset, the chirality angle is computed for each voxel. The angles are binned and plotted in a histogram. To determine the depth dependence, the data are plotted with one line for each depth resolved layer. In this system, the chirality is constantly maximum at 180°, indicating a positive Néel profile across the depth (Fig. 3D). The consistent Néel profile is what theory predicts for a multilayer system.

3D resolved PMA, exchange, and DMI

A 3D measurement makes computation of micromagnetic energy densities possible. Unlike in a 2D projection where 3D information can only be inferred, a direct 3D measurement allows vector quantities related to terms in the micromagnetic Hamiltonian to be computed from data. Here, we compare the contributions of competing magnetic interactions namely symmetric exchange $-A(\nabla \cdot \mathbf{m})^2$, antisymmetric exchange or DMI $-\vec{D} \bullet (\mathbf{m}_i \times \mathbf{m}_j)$ (13, 15), and uniaxial anisotropy $-K(\hat{z} \bullet \mathbf{m})^2$. While this technique cannot measure the constants A, D, and K directly, the values of vector operations on the data can be reported, allowing us to spatially map the different energy densities. The energy profiles (Fig. 4) are normalized to equal area under the curve. Estimates of the micromagnetic constants themselves are provided in Fig. 3C based on a curve fitting approach on the topological charge profile. Similar to the topological charge, the energy densities do not have perfect radial symmetry (Fig. 4, A to C). For a more parsimonious representation that does not capture the variations from radial symmetry, in Fig. 4 (D to F), we take the average topological charge at each radius.

Taking vector operations on the data shows the domain wall to be the region of maximal DMI and PMA, while exchange energy is more localized to the core of the skyrmion (Fig. 4, A to C). At the core of the skyrmion, the divergence of the vector field is the largest, leading to a maximum Heisenberg exchange contribution. In the domain wall, the in-plane spins are unfavorably aligned with the easy out-of-plane axis leading to a large accumulation of PMA energy. The DMI, however, lowers the energy of the domain wall as the vector $\vec{D}$ is in-plane for this multilayer system making energetic contributions to the azimuthally symmetric spins canting across the domain wall.
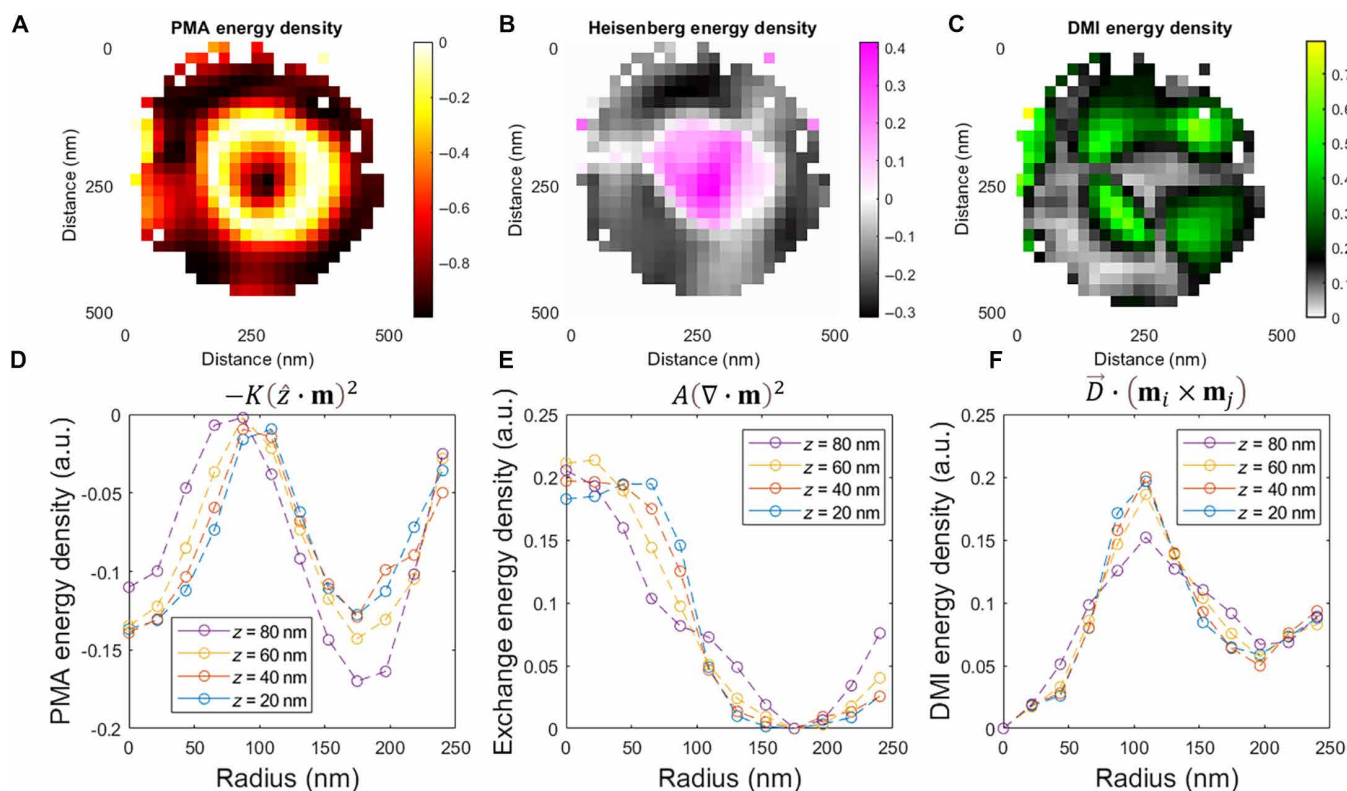
Fig. 4. Energy densities. (**A**) z-averaged PMA energy image with radial average for each individual 20-nm-thick vertical slice. The energy is determined at the level of a relative normalized spatial density of the z component squared of the magnetization, $-K(\hat{z} \bullet \mathbf{m})^2$. (**B**) z-averaged exchange energy image with radial average for each individual 20-nm-thick vertical slice. The energy is determined at the level of a relative normalized spatial density of the divergence squared of the magnetization, $A(\nabla \cdot \mathbf{m})^2$. (**C**) z-averaged DMI energy image with radial average for each individual 20-nm-thick vertical slice. The energy is determined at the level of a relative normalized spatial density of the interfacial chiral–type ordering, $\vec{D} \bullet (\mathbf{m}_i \times \mathbf{m}_j)$ where $\vec{D}$ is a unit vector perpendicular to the displacement between spin cells, lying in-plane. (**D**) Radially averaged, normalized to area under curve PMA energy density profile [arbitrary units (a.u.)]. (**E**) Radially averaged, normalized to area under curve exchange interaction energy density profile (a.u.). (**F**) Radially averaged, normalized to area under curve DMI energy density profile (a.u.).

Along the z profile, the calculated second-principal energy densities are nonuniform (Fig. 4, D to F). This suggests that the fundamental energetic interactions are nonuniform across the depth profile. This may be related to atomic-scale roughness or pinning defects. The emergent consequence of the changing energetic densities is that the skyrmion profile evolves with depth (Fig. 3A). However, the change in local energy density does not appear to affect the chirality of the skyrmion (Fig. 3D).

With this technique, the energy can only be determined at the level of spatial distribution. Knowledge of the magnetization field alone is not enough to directly determine values of micromagnetic constants, which are determined by both spin and orbital ordering on atomic length scales. Estimating energetic properties from direct vector operations cannot determine behavior below the ~20-nm voxel size where interlayer coupling is relevant, and it cannot account for nonlinear interactions between energetic terms.

DISCUSSION

Using soft x-ray laminography, we have obtained the 3D structure of a skyrmion in a magnetic multilayer disk at ~20-nm voxel size. From the data, the topological skyrmion number is computed directly, and the profile of the spin texture is probed at a length scale comparable to micromagnetic simulations. With direct vector operations on the data, the spatial distributions of different energetic interactions are estimated, and it is found that the DMI energy density is largest in the domain wall, while the Heisenberg exchange energy density is more localized to the center of the structure. With another approach, the effects of altering energy terms on the topological charge profile is to make the topological charge profile steeper in the case of a greater PMA-to-DMI ratio. This is reflected in the data suggesting that the interactions in the sample are not uniform over the depth profile.

This technique could be equally applied to larger multidomain and multi-skyrmion string samples (26). Soft x-rays have the advantage of large magnetic contrast at the L edges particularly in transition metals allowing for a wide range of sample compositions. Similar analysis of topological charge could be applied to other skyrmion phases including skyrmions strings and chiral bobbers (1, 2, 27).

The acquisition time of STXM for such a tilt series, around 12 hours, is faster than diffraction-based techniques such as soft-x-ray ptychography. Limitations for the soft x-ray approach come from sample thicknesses greater than several hundred nanometers where absorption length of soft x-rays is no longer sufficient. At these thicknesses, hard x-rays or neutrons are a possibility although they have much lower magnetic contrast (28). In addition, the single 45° incident angle leads to a missing wedge of spatial information, making the technique best suited for planar or tubular samples (29).

This work establishes that soft x-ray laminography using STXM has reached a level of maturity to probe magnetic systems at the same level as ubiquitous micromagnetic simulations with quantitative measurements of topological features, which vary across depth. This level of sophistication in measurement and analysis will be necessary to probe the configuration space of material design for more complex 3D textures such as hopfions. Our results provide the foundation for nanoscale magnetic metrology for future tailored spintronics devices using topology as a design parameter.

MATERIALS AND METHODS

Sample synthesis and patterning

The trilayer film samples were deposited by DC magnetron sputtering onto a 100-nm-thin SiNx membrane. The trilayer film of $10 \times$ [Ir (1 nm)/Co (1 nm)/Pt (1 nm)]/$10 \times$ [Ir (1 nm)/Co (1.5 nm)/Pt (1 nm)]/$10 \times$ [Ir (1 nm)/Co (1 nm)/Pt (1 nm)] with a total thickness of 95 nm (Fig. 1A) was chosen in view of a suitable x-ray absorption for soft x-rays around a photon energy of 778 eV, corresponding to the Co L_3 absorption edge. Characterization of the unpatterned multilayer with magnetic force microscopy shows complex domain structures in the variable Co thickness film (Fig. 1B). Previous studies have observed target skyrmions and hopfions in similar multilayers (3, 14). To confine the domain patterns on the nanoscale, the multilayers were patterned into disks with diameters ranging from 200 to 1000 nm by electron beam lithography, followed by lift-off. Although, in the x-ray laminography experiments, we observe a skyrmion spin texture rather than a hopfion or target skyrmion, our approach to quantitatively analyzing the 3D spin texture will be equally applicable in those textures as well.

3D tomography with soft x-ray laminography

The soft x-ray magnetic laminography experiments were conducted at the PolLux beamline of the Swiss Light Source at PSI in Villigen/Switzerland. A rotation series at 45° sample incident angle to the x-ray beam was taken over 56 rotation angles covering 360° with data taken over a 12-hour period. Three laminography datasets were recorded at the L_3 edge of Co (around 778-eV x-ray photon energy) with both positive, $I_\uparrow$, and negative circular polarization, $I_\downarrow$, as well as linear horizontal polarization. All three images are necessary at each rotation angle. The two circular polarization images allow to quantitatively derive the x-ray magnetic circular dichroism (XMCD) signal, whereas the linearly polarized x-ray image enables removing additional nonlinear structural background signals not accounted for with the typical dichroism $I_{\mathrm{XMCD}} = \frac{I_\uparrow - I_\downarrow}{I_\uparrow + I_\downarrow}$, as well as unwanted asymmetries in the degree of circular polarization of the beam produced by the PolLux bending magnet (30, 31). The step size in the horizontal and vertical direction was 20 nm. This step size effectively oversamples the diffraction-limited resolution, which is 42.7 nm as calculated from end-station geometry and optics of the 35-nm zone plate that was used during the experiment. Oversample scans were not taken because of the long acquisition times required for this technique.

Supplementary Materials

This PDF file includes:
Supplementary Text
Figs. S1 and S2

REFERENCES AND NOTES

1. M. T. Birch, D. Cortés-Ortuño, L. A. Turnbull, M. N. Wilson, F. Groß, N. Träger, A. Laurenson, N. Bukin, S. H. Moody, M. Weigand, G. Schütz, H. Popescu, R. Fan, P. Steadman, J. A. T. Verezhak, G. Balakrishnan, J. C. Loudon, A. C. Twitchett-Harrison, O. Hovorka, H. Fangohr, F. Y. Ogrin, J. Gräfe, P. D. Hatton, Real-space imaging of confined magnetic skyrmion tubes. *Nat. Commun.* **11**, 1726 (2020).
2. D. Wolf, S. Schneider, U. K. Rößler, A. Kovács, M. Schmidt, R. E. Dunin-Borkowski, B. Büchner, B. Rellinghaus, A. Lubk, Unveiling the three-dimensional magnetic texture of skyrmion tubes. *Nat. Nanotechnol.* **17**, 250–255 (2022).
3. N. Kent, N. Reynolds, D. Raftrey, I. T. G. Campbell, S. Virasawmy, S. Dhuey, R. V. Chopdekar, A. Hierro-Rodriguez, A. Sorrentino, E. Pereiro, S. Ferrer, F. Hellman, P. Sutcliffe, P. Fischer,

Creation and observation of hopfions in magnetic multilayer systems. *Nat. Commun.* **12**, 1562 (2021).

4. F. Zheng, N. S. Kiselev, F. N. Rybakov, L. Yang, W. Shi, S. Blügel, R. E. Dunin-Borkowski, Hopfion rings in a cubic chiral magnet. *Nature* **623**, 718–723 (2023).

5. M. Grelier, F. Godel, A. Vecchiola, S. Collin, K. Bouzehouane, A. Cros, N. Reyren, R. Battistelli, H. Popescu, C. Léveillé, N. Jaouen, F. Büttner, X-ray holography of skyrmionic cocoons in aperiodic magnetic multilayers. *Phys. Rev. B* **107**, L220405 (2023).

6. C. Donnelly, K. L. Metlov, V. Scagnoli, M. Guizar-Sicairos, M. Holler, N. S. Bingham, J. Raabe, L. J. Heyderman, N. R. Cooper, S. Gliga, Experimental observation of vortex rings in a bulk magnet. *Nat. Phys.* **17**, 316–321 (2021).

7. S. Das, Y. L. Tang, Z. Hong, M. A. P. Gonçalves, M. R. McCarter, C. Klewe, K. X. Nguyen, F. Gómez-Ortiz, P. Shafer, E. Arenholz, V. A. Stoica, S.-L. Hsu, B. Wang, C. Ophus, J. F. Liu, C. T. Nelson, S. Saremi, B. Prasad, A. B. Mei, D. G. Schlom, J. Íñiguez, P. García-Fernández, D. A. Muller, L. Q. Chen, J. Junquera, L. W. Martin, R. Ramesh, Observation of room-temperature polar skyrmions. *Nature* **568**, 368–372 (2019).

8. C. Donnelly, A. Hierro-Rodríguez, C. Abert, K. Witte, L. Skoric, D. Sanz-Hernández, S. Finizio, F. Meng, S. McVitie, J. Raabe, D. Suess, R. Cowburn, A. Fernández-Pacheco, Complex free-space magnetic field textures induced by three-dimensional magnetic nanostructures. *Nat. Nanotechnol.* **17**, 136–142 (2022).

9. A. Rana, C.-T. Liao, E. Iacocca, J. Zou, M. Pham, X. Lu, E.-E. C. Subramanian, Y. H. Lo, S. A. Ryan, C. S. Bevis, R. M. Karl, A. J. Glaid, J. Rable, P. Mahale, J. Hirst, T. Ostler, W. Liu, C. M. O'Leary, Y.-S. Yu, K. Bustillo, H. Ohldag, D. A. Shapiro, S. Yazdi, T. E. Mallouk, S. J. Osher, H. C. Kapteyn, V. H. Crespi, J. V. Badding, Y. Tserkovnyak, M. M. Murnane, J. Miao, Three-dimensional topological magnetic monopoles and their interactions in a ferromagnetic meta-lattice. *Nat. Nanotechnol.* **18**, 227–232 (2023).

10. O. M. Volkov, O. V. Pylypovskyi, F. Porrati, F. Kronast, J. A. Fernandez-Roldan, A. Kákay, A. Kuprava, S. Barth, F. N. Rybakov, O. Eriksson, S. Lamb-Camarena, P. Makushko, M.-A. Mawass, S. Shakeel, O. V. Dobrovolskiy, M. Huth, D. Makarov, Three-dimensional magnetic nanotextures with high-order vorticity in soft magnetic wireframes. *Nat. Commun.* **15**, 2193 (2024).

11. H. Jani, J. Harrison, S. Hooda, S. Prakash, P. Nandi, J. Hu, Z. Zeng, J.-C. Lin, C. Godfrey, G. J. Omar, T. A. Butcher, J. Raabe, S. Finizio, A. V.-Y. Thean, A. Ariando, P. G. Radaelli, Spatially reconfigurable antiferromagnetic states in topologically rich free-standing nanomembranes. *Nat. Mater.* **23**, 619–626 (2024).

12. D. Raftrey, P. Fischer, Advanced magnetic x-ray spectro-microscopies to characterize mesoscopic magnetic materials. *J. Magn. Magn. Mater.* **545**, 168734 (2022).

13. C. Moreau-Luchaire, C. Moutafis, N. Reyren, J. Sampaio, C. A. F. Vaz, N. Van Horne, K. Bouzehouane, K. Garcia, C. Deranlot, P. Warnicke, P. Wohlhüter, J.-M. George, M. Weigand, J. Raabe, V. Cros, A. Fert, Additive interfacial chiral interaction in multilayers for stabilization of small individual skyrmions at room temperature. *Nat. Nanotechnol.* **11**, 444–448 (2016).

14. N. Kent, R. Streubel, C.-H. Lambert, A. Ceballos, S.-G. Je, S. Dhuey, M.-Y. Im, F. Büttner, F. Hellman, S. Salahuddin, P. Fischer, Generation and stability of structurally imprinted target skyrmions in magnetic multilayers. *Appl. Phys. Lett.* **115**, 112404 (2019).

15. F. Hellman, A. Hoffmann, Y. Tserkovnyak, G. S. D. Beach, E. E. Fullerton, C. Leighton, A. H. MacDonald, D. C. Ralph, D. A. Arena, H. A. Dürr, P. Fischer, J. Grollier, J. P. Heremans, T. Jungwirth, A. V. Kimel, B. Koopmans, I. N. Krivorotov, S. J. May, A. K. Petford-Long, J. M. Rondinelli, N. Samarth, I. K. Schuller, A. N. Slavin, M. D. Stiles, O. Tchernyshyov, A. Thiaville, B. L. Zink, Interface-induced phenomena in magnetism. *Rev. Mod. Phys.* **89**, 25006 (2017).

16. A. Hrabec, N. A. Porter, A. Wells, M. J. Benitez, G. Burnell, S. McVitie, D. McGrouther, T. A. Moore, C. H. Marrows, Measuring and tailoring the Dzyaloshinskii-Moriya interaction in perpendicularly magnetized thin films. *Phys. Rev. B* **90**, 20402 (2014).

17. C. Donnelly, S. Gliga, V. Scagnoli, M. Holler, J. Raabe, L. J. Heyderman, M. Guizar-Sicairos, Tomographic reconstruction of a three-dimensional magnetization vector field. *New J. Phys.* **20**, 083009 (2018).

18. C. Donnelly, S. Finizio, S. Gliga, M. Holler, A. Hrabec, M. Odstrčil, S. Mayr, V. Scagnoli, L. J. Heyderman, M. Guizar-Sicairos, J. Raabe, Time-resolved imaging of three-dimensional nanoscale magnetization dynamics. *Nat. Nanotechnol.* **15**, 356–360 (2020).

19. G. Chen, T. Ma, A. T. N'Diaye, H. Kwon, C. Won, Y. Wu, A. K. Schmid, Tailoring the chirality of magnetic domain walls by interface engineering. *Nat. Commun.* **4**, 2671 (2013).

20. M. Heigl, S. Koraltan, M. Vaňatka, R. Kraft, C. Abert, C. Vogler, A. Semisalova, P. Che, A. Ullrich, T. Schmidt, J. Hintermayr, D. Grundler, M. Farle, M. Urbánek, D. Suess, M. Albrecht, Dipolar-stabilized first and second-order antiskyrmions in ferrimagnetic multilayers. *Nat. Commun.* **12**, 2611 (2021).

21. A. Hierro-Rodriguez, C. Quirós, A. Sorrentino, L. M. Alvarez-Prado, J. I. Martín, J. M. Alameda, S. McVitie, E. Pereiro, M. Vélez, S. Ferrer, Revealing 3D magnetization of thin films with soft x-ray tomography: Magnetic singularities and topological charges. *Nat. Commun.* **11**, 6382 (2020).

22. E. Burgos-Parra, Y. Sassi, W. Legrand, F. Ajejas, C. Léveillé, P. Gargiani, M. Valvidares, N. Reyren, V. Cros, N. Jaouen, S. Flewett, Probing of three-dimensional spin textures in multilayers by field dependent x-ray resonant magnetic scattering. *Sci. Rep.* **13**, 11711 (2023).

23. M. Di Pietro Martínez, A. Wartelle, C. Herrero Martínez, F. Fettar, F. Blondelle, J.-F. Motte, C. Donnelly, L. Turnbull, F. Ogrin, G. van der Laan, H. Popescu, N. Jaouen, F. Yakhou-Harris, G. Beutier, Three-dimensional tomographic imaging of the magnetization vector field using Fourier transform holography. *Phys. Rev. B* **107**, 094425 (2023).

24. P. Fischer, M.-Y. Im, S. Kasai, K. Yamada, T. Ono, A. Thiaville, X-ray imaging of vortex cores in confined magnetic structures. *Phys. Rev. B* **83**, 212402 (2011).

25. S. Zhang, J. Zhang, Y. Wen, E. M. Chudnovsky, X. Zhang, Determination of chirality and density control of Néel-type skyrmions with in-plane magnetic field. *Commun. Phys.* **1**, 36 (2018).

26. S. Seki, M. Suzuki, M. Ishibashi, R. Takagi, N. D. Khanh, Y. Shiota, K. Shibata, W. Koshibae, Y. Tokura, T. Ono, Direct visualization of the three-dimensional shape of skyrmion strings in a noncentrosymmetric magnet. *Nat. Mater.* **21**, 181–187 (2022).

27. F. Zheng, F. N. Rybakov, A. B. Borisov, D. Song, S. Wang, Z.-A. Li, H. Du, N. S. Kiselev, J. Caron, A. Kovács, M. Tian, Y. Zhang, S. Blügel, R. E. Dunin-Borkowski, Experimental observation of chiral magnetic bobbers in B20-type FeGe. *Nat. Nanotechnol.* **13**, 451–455 (2018).

28. M. E. Henderson, B. Heacock, M. Bleuel, D. G. Cory, C. Heikes, M. G. Huber, J. Krzywon, O. Nahman-Levesqué, G. M. Luke, M. Pula, D. Sarenac, K. Zhernenkov, D. A. Pushin, Three-dimensional neutron far-field tomography of a bulk skyrmion lattice. *Nat. Phys.* **19**, 1617–1623 (2023).

29. P. Pip, S. Treves, J. R. Massey, S. Finizio, Z. Luo, A. Hrabec, V. Scagnoli, J. Raabe, L. Philippe, L. J. Heyderman, C. Donnelly, X-ray imaging of the magnetic configuration of a three-dimensional artificial spin ice building block. *APL Mater.* **10**, 101101 (2022).

30. B. Watts, S. Finizio, K. Witte, M. Langer, S. Mayr, S. Wintz, B. Sarafimov, J. Raabe, Status of the PolLux STXM beamline. *Microsc. Microanal.* **24**, 476–477 (2018).

31. K. Witte, A. Späth, S. Finizio, C. Donnelly, B. Watts, B. Sarafimov, M. Odstrcil, M. Guizar-Sicairos, M. Holler, R. H. Fink, J. Raabe, From 2D STXM to 3D imaging: Soft x-ray laminography of thin specimens. *Nano Lett.* **20**, 1305–1314 (2020).